

SUPPLEMENTAL MATERIAL

Rapid retreat of the southwestern Laurentide Ice Sheet during the Bølling-Allerød interval

Sophie L. Norris, Lev Tarasov, Alistair J. Monteath, John C. Gosse, Alan J. Hidy, Martin Margold and Duane G. Froese

*Corresponding author: slnorris@ualberta.ca, duane.froese@ualberta.ca

Methods

Cosmogenic nuclide exposure dating

Laboratory methods

26 boulder samples were collected for cosmogenic exposure dating using ^{10}Be at five site locations. These included: four from the Pine Lake Moraine (PLM), six from gravel bars within the Beaver River Spillway (BR), five from erosional residuals at the head of the Clearwater Athabasca Spillway (CLAS), five from the Cree Lake Moraine (CLM) and six from the western and eastern parts of the upper-Cree Lake Moraine (UCLM-W and UCLM-E). Samples reflect erosion residuals and gravel bars were formed by catastrophic outburst floods that drained, contemporaneous with ice retreat, from ice dammed lakes (see Norris et al., 2019, 2021). Samples were collected for exposure dating with a diamond blade cutoff saw or hammer and chisel. The sampled erratics consist of Precambrian rocks from the Athabasca Group sandstone and granites from the Canadian Shield. All samples were prepared as BeO targets at CRISDal Lab, Dalhousie University. To facilitate isolation of sufficient quartz, the following laboratory techniques were employed.

The samples were cleaned, crushed, and ground, and the 250-355 μm fraction was rinsed, leached in aqua regia (2 hours), and etched in HF, before mineral separation using combinations of froth floatation, Frantz magnetic separation, air abrasion, heavy liquids, and controlled digestions of non-quartz phases using hydrofluoric or hexafluorosilicic acids. When the quartz concentrate was sufficiently pure (as determined optically and with <100 ppm Al and Ti as determined on a 1 g aliquot with the lab's ICP-OES), approximately 35 wt% of the dried quartz concentrate was removed over three digestion-rinse cycles using an ultrasonic bath with dilute HF as per Kohl and Nishiizumi (1992). The samples were spiked with approximately 240 μg of

the lab's BeCl₂ carrier ('Be-Carrier-31-28Sept2012'; prepared from a deeply mined Ural Mountain phenacite with ¹⁰Be/⁹Be below 1 x 10⁻¹⁶), and were digested in a HF-HNO₃ mixture, evaporated twice in perchloric acid, and treated with anion and cation column chemistry to isolate the Be²⁺. After acidifying with perchloric and nitric acid to remove residual B, Be(OH)₂ was precipitated using ultrapure ammonia gas, transferred to a cleaned boron-free quartz vial and carefully calcined in a Bunsen burner flame to a white oxide for over three minutes. In an antistatic glovebox the BeO was powdered, mixed 2:3 by volume with high purity niobium powder (325 mesh), and packed into stainless steel cathodes for ¹⁰Be/⁹Be measurement at the Center for Accelerator Mass Spectrometry, Lawrence Livermore National Lab (CAMS-LLNL). These measurements were made against the 07KNSTD3110 standard with a known ¹⁰Be/⁹Be of 2850x10⁻¹⁵ (Nishiizumi et al. 2007). Process blanks were also analysed and used (average 1 blank per 8 samples) to subtract ¹⁰Be introduced during target preparation and analysis. For all samples, this correction was less than 1% of the adjusted ¹⁰Be values.

Age calculation

Exposure ages were calculated using the 'age calculator formerly known as CRONUS-Earth Online Exposure Age Calculator' (Balco et al., 2008; v3.0; constraints 3.0.3, at https://hess.ess.washington.edu/math/v3/v3_age_in.html) using the default calibration set of Borchers et al. (2016) and the time dependent 'LSDn' production scaling scheme of Lifton et al. (2014). Utilizing other scaling schemes or production rates does not alter our conclusions as the ages are within the internal uncertainty of our reported ages (Table DR1). Various factors control the cosmic ray flux to the boulder and therefore causing the calculated exposure ages to underestimate or overestimate the timing of ice marginal retreat at a site. Factors that will cause exposure ages to underestimate the age of retreat besides inheritance of cosmogenic ¹⁰Be from exposure prior to deposition:

1. Snow and ice cover

The history of precipitation throughout the study area is uncertain, let alone the height and density of snow or ice cover which can be quite variable depending on local conditions (solar attitude, wind speed and direction, local and micro-topography, and vegetation). In the rain shadow of the Rocky Mountains, the study region currently has low winter

precipitation, and because the sampled boulder surfaces are mostly 0.5 m above ground level (mean=90 cm, median=82 cm, min=30 cm, max=160 cm above local ground level, only one boulder <50 cm), Table DR1) and situated on open plains or ridge tops, we would expect boulders to be windswept of snow or ice cover. Nevertheless, we tested the sensitivity of snow or ice shielding by using the climate normals data for a representative location inside the field area (Fort McMurray Airport, Alberta, 56.65°N, 111.22°W, 368 m asl) which has an elevation within 200 m of most samples (except for the Pine Lake moraine samples which are 926 m). The normals data indicate no month with an average snow depth >30 cm, although an extreme snow depth of 68 cm was recorded on Jan 2, 1968. Nevertheless, while most of the boulders are above that snow height, boulders would have still carried some snow cover. The mean snow depth is 25 cm in the four months with the greatest mean snow depth. Assuming that every boulder was covered by this amount for the four months every year since exposure began, and that the average snow density for the region is 0.224 gcm⁻³ (Williams, 1956), the shielding effect would be to decrease average ¹⁰Be production rate by 3.66%. However, given the boulder height and exposed position of the boulders which would cause snow cover to be thinner and shorter, this is likely a significant overestimate, and the actual effect of snow or firn cover is less than 2%, i.e. the unadjusted exposure age could be an under-estimated by up to 2%. Wind speed and tree cover can also affect this estimate.

2. Tree shielding

The effect of tree shielding is difficult to estimate not only because it varies with time (and forest cover at each of the sample sites over the past 15 kyr is not certain), but it varies with forest density, forest type, fire frequency, and other factors (Plug et al., 2007). Plug et al. indicate that a temperate boreal forest may contribute as much as 2% shielding, and as most of the sample locations did not experience such a dense forest cover over the exposure duration (e.g. Ritchie, 1976) the average effect would likely be to underestimate the exposure age by < 1%.

3. Erosion

As indicated, the sampling strategy optimizes the collection of boulders with no evidence of erosion. Therefore, there may not have been any erosion. However, allowing for an average erosion rate for granitoid lithologies of 1 mm/kyr (Zimmerman et al., 1994; Blackwelder,

1978), and knowing the impact of erosion on exposure age will increase with exposure time, we compared the exposure ages calculated assuming both 0 and 1 mm/kyr. If the exposure history was adjusted for a 1 mm/kyr erosion rate, the exposure age would increase by an average of 1.0% (0.4% for the 6 kyr exposure, and 1.3% for the 16 kyr exposure). We cannot preclude that the boulders exhumed through some sediment cover (e.g. by frost heave or sediment erosion). However, because the boulders are relatively large and high, the terrain gently sloped, and the ages at each site relatively consistent and show no correlation with boulder height, we suggest that if boulder exhumation did occur it would have been early in the exposure history and not a significant impact on the ^{10}Be production history.

4. Atmospheric pressure changes

The mass of the atmosphere above a sample controls the energy spectrum and flux of secondary cosmic radiation to a boulder. Glacial isostatic adjustment (GIA) of the region, resulting from the depression of the land surface by a >1.5 km thick continental ice sheet (Lambeck et al., 2017), affects the elevation and thus controls atmospheric thickness and secondary cosmic radiation shielding (Jones et al., 2017). Unlike snow or tree cover which have a large uncertainty owing to the lack of precise paleoclimate or paleovegetation data for each of the field areas, there is no doubt that some isostatic adjustment has occurred. The question is the magnitude and the change in the rate of surface uplift over the exposure history. As the study areas are not at the LGM limits of the LIS, post-glacial GIA here would mean that the production rate for the modern position of each boulder is overestimated and the exposure age is therefore underestimated. Correcting for a thicker atmospheric shielding early in the exposure history would therefore cause the adjusted ages to be slightly older, as with erosion or shielding. We apply a GIA correction using numerical model simulations of Tarasov et al. (2012) to determine the average elevation of the sample site since deglaciation. We calculate the elevation for each sample site at 1000 yr intervals, from ice free conditions within the model to 0 yrs, using dRSL data (Tarasov et al., 2012). Based on 1000 yr interval elevations we calculate a average dRSL for each sample site for this deglacial period. We then correct the modern elevation of our sample sites by the average deglacial dRSL elevation before the exposure age was calculated.

A GIA correction using alternative numerical model simulations (e.g. Lambeck et al., 2017; see Table DR1) display consistent results. The GIA-corrected exposure ages (e.g. Table SD1, $^{10}\text{Be}^b$) range from 8% to 3% older than the calculation without considering GIA ($^{10}\text{Be}^a$) depending on the exposure duration. While this is a significant systematic error, it is very ice-sheet model dependent, and ignores the many complex changes in atmospheric pressure related to katabatic winds off both ice sheets, changes in the density distribution of the atmosphere with global temperature, and more complex changes related to the impact of ice sheet geometry on atmospheric dynamics (Staiger et al., 2007). Using a global climate-model coupled with an ice sheet model, Staiger et al. (2007) showed that the atmospheric effect at high altitudes (Himalaya, ignoring GIA) would cause the production rate to be $6.5 \pm 1.5\%$ greater during the LGM than today, but after the LGM the effect on time-integrated production rate would decrease and result in a total effect of 3% higher post-LGM time-integrated production rate than at that site today. The total effect at lower elevations and after the LGM such as this study will be less, but the complications related to the presence of ice sheets are difficult to assess. A further consideration is that while dRSL increments can be interpreted from various global datasets, the effect of a lower sea level and the displacement of atmosphere by ice sheets (Osmaston, 2005) also complicates the modeling of the atmospheric dynamics above land. Therefore, while the GIA adjustments may have contributed percent-level increases in the production rate of a boulder over time, the uncertainty in correcting time-average atmospheric shielding requires future effort to refine.

Compilation of pre-existing chronology

We compile a dataset of pre-existing luminescence, ^{10}Be surface exposure ages and ‘high quality’ minimum radiocarbon chronologies. Individual dates are summarised in Table 3.

Pre-existing ^{10}Be surface exposure ages are limited to a single study (Margold et al., 2019) in the region. 16 glacial erratic boulders that mark the zone of coalescence of the Laurentide and Cordilleran Ice Sheet have been recently re-dated (Margold et al., 2019) using ^{10}Be surface exposure ages. Of the 16 boulders dated, 12 accurately constrain the age of decoupling of the two ice sheets and are used by the original authors to provide a weighted mean age, including

propagated uncertainty, of $14,900 \pm 900$ cal yr BP. We present these dates at one standard deviation uncertainty consistent with our samples.

Optically stimulated luminescence (OSL) and infrared stimulated luminescence (IRSL), from eolian sands have been previously used to constrain deglaciation within the study region (Wolfe et al., 2004; Munyikwa et al., 2011, 2017). We collate dates and group them into sites within 30km and present the oldest reliable sites where several exist within a 40 km region. We remove outliers proposed by the original authors and present dates with one standard deviation uncertainty.

A large number of ^{14}C dates (see DR3) have been used to constrain the deglaciation of the southwestern sector of the LIS. We focus on ‘high quality’ minimum limiting ^{14}C chronologies and present the five oldest reliable dates from within a 40 km region. We exclude dates on bulk sediments, terrestrial shells or mixed assemblages. Where available Accelerator Mass Spectrometry (AMS) ^{14}C dates are prioritized over radiometric (conventional) dating methods. In cases of bone, ultrafiltered collagen samples, where available, are prioritized. We remove outliers proposed by the original authors or where later data complications make clear arguments for the exclusion of single unreproduced dates. Radiocarbon dates are recalibrated using the northern hemisphere IntCal20 calibration curve (Reimer et al., 2020) and presented at two standard deviation uncertainty.

Bayesian age modelling

We integrate luminescence dates (OSL/ IRSL), ^{10}Be exposure ages and ^{14}C dates within a Bayesian age model using OxCal v.4.4 (Bronk Ramsey, 2009a). The model uses the known sequence of ice-retreat, across the western Interior Plains (southwest-northeast demarcated by recessional moraines), as a ‘prior model’ and follows the sampling transect of cosmogenic ^{10}Be exposure dates from this study. The existing luminescence and five oldest ^{14}C -dates from a single landform, or within a 40 km region, are treated at site level similar to the cosmogenic data.

Within the *Sequence* model we place dates associated with the Foothills Erratics Train and the Cree Lake Moraine in continuous *Phases*, with no defined (stratigraphic or temporal) internal

order. We took this approach as the Foothills Erratics Train was sampled following the CIS/LIS saddle (Margold et al., 2019), while dates from the Cree Lake Moraine closely overlap and represent a prolonged still-stand. These *Phases* were separated by *Boundaries* which allowed us to quantify ‘start’ and ‘end’ dates for the Cree Lake Moraine emplacement (Bronk Ramsey, 2009a). Because ^{14}C ages do not directly date ice-retreat, but the age of organic carbon deposited an indeterminable amount of time after the ice has melted, ^{14}C dates were integrated into the model using the *Before* function which treats the data as minimum (*terminus ante quem*) age controls only. This approach was necessary as large numbers of comparatively precise ^{14}C dates could not be reconciled with luminescence and ^{10}Be exposure ages which were typically older than the ^{14}C measurements, and more closely date the timing of deglaciation.

Prior to model construction anomalous ^{14}C -dates from bulk sediments, terrestrial shells or mixed assemblages were manually excluded (see above) from the database and were not included in the *Sequence* model. A ‘general’ *Outlier_Model* was applied with a 5% chance of any date being an outlier. Statistical outliers that should be considered for rejection were identified using Agreement index values (<60%); however, dates were only removed if they reduced the overall Agreement Index of the model to below the recommended 60% threshold (Bronk Ramsey, 2009b). In practice, the manual filtering of anomalous data, treatment of ^{14}C dates as minimum ages and the large uncertainties associated with luminescence and ^{10}Be exposure ages meant that no dates needed to be removed from the Bayesian model.

Modelling of ice retreat and meltwater equivalent

We reran the two best-fitting North American ice-sheet model simulations of Tarasov et al. (2012) to estimate the rate of ice volume loss and equivalent sea level contribution from the SWLIS based on our new chronology. The original simulations were derived from an approximate Bayesian calibration of a glaciological model against a large set of geological and geophysical constraints. The model included 39 ensemble parameters that were calibrated to address uncertainties in climate forcing, basal drag, ice calving, and the amount of nudging towards the input target ice margin chronologies from Dyke (2004) (interpolated between available time-slices). The total amount of nudging is a part of the misfit score for the calibration and thereby the calibration endeavored to minimize the amount of nudging required. The

chronological acceleration of the target chronology was progressively increased from 21ka (calendar) to a maximum acceleration of 2.0 kyr (shifting the original 18.3 ka isochrone to 16.3 ka) then progressively relaxed to line back up at 9.28 ka. A mean ice sheet retreat rate was calculated using multiple transects, taken at 100 km intervals, perpendicular to ice retreat direction across the SWLIS. In order to further assess the connection between SWLIS ice retreat rates and rapid Bølling-Allerød warming a fully coupled ice/climate modelling should be applied.

SUPPLEMENTAL REFERENCES

- Balco, G., Stone, J. O., Lifton, N. A., and Dunai, T. J. 2008: A complete and easily accessible means of calculating surface exposure ages or erosion rates from ^{10}Be and ^{26}Al measurements. *Quaternary geochronology*, 3(3), 174-195. <https://doi.org/10.1016/j.quageo.2007.12.001>
- Benedict, J.B. 1993: Influence of snow upon rates of granodiorite weathering, Colorado Front Range, USA. *Boreas*, 22(2), 87-92. <https://doi.org/10.1111/j.1502-3885.1993.tb00167.x>
- Borchers, B., Marrero, S., Balco, G., Caffee, M., Goehring, B., Lifton, N., Nishiizumi, K., Phillips, F., Schaefer, J. and Stone, J. 2016: Geological calibration of sp ation production rates in the CRONUS-Earth project. *Quaternary Geochronology* 31, 188–198. <https://doi.org/10.1016/j.quageo.2015.01.009>
- Bronk Ramsey, C., 2009a: Bayesian analysis of radiocarbon dates. *Radiocarbon*, 51(1), 337-360. <https://doi.org/10.1017/S0033822200033865>
- Bronk Ramsey, C., 2009b: Dealing with outliers and offsets in radiocarbon dating. *Radiocarbon*, 51(3), 1023-1045. <https://doi.org/10.1017/S0033822200034093>
- Jones, R.S., Whitehouse, P.L., Bentley, M.J., Small, D. and Dalton, A.S. 2019: Impact of glacial isostatic adjustment on cosmogenic surface-exposure dating. *Quaternary Science Reviews*, 212, 206-212. <https://doi.org/10.1016/j.quascirev.2019.03.012>
- Kohl, C. P., and Nishiizumi, K. 1992: Chemical isolation of quartz for measurement of in-situ-produced cosmogenic nuclides. *Geochimica et Cosmochimica Acta*, 56(9), 3583-3587.
- Lal, D. 1991: Cosmic ray labeling of erosion surfaces: in situ nuclide production. *Earth and Planetary Science Letters*, 104, 424-439. [https://doi.org/10.1016/0016-7037\(92\)90401-4](https://doi.org/10.1016/0016-7037(92)90401-4)
- Lambeck, K., Purcell, A., and Zhao, S. 2017: The North American Late Wisconsin ice sheet and mantle viscosity from glacial rebound analyses. *Quaternary Science Reviews*, 158, 172-210. <https://doi.org/10.1016/j.quascirev.2016.11.033>

Lifton, N., Sato, T., and Dunai, T. J. 2014: Scaling in situ cosmogenic nuclide production rates using analytical approximations to atmospheric cosmic-ray fluxes. *Earth and Planetary Science Letters*, 386, 149-160. <https://doi.org/10.1016/j.epsl.2013.10.052>

Margold, M., Gosse, J. C., Hidy, A. J., Woywitka, R. J., Young, J. M. and Froese, D. 2019: Beryllium-10 dating of the Foothills Erratics Train in Alberta, Canada, indicates detachment of the Laurentide Ice Sheet from the Rocky Mountains at ~15 ka. *Quaternary Research*, 92(2), 469-482. <https://doi.org/10.1017/qua.2019.10>

Munyikwa, K., Feathers, J. K., Rittenour, T. M., and Shrimpton, H. K. 2011: Constraining the Late Wisconsinan retreat of the Laurentide ice sheet from western Canada using luminescence ages from postglacial aeolian dunes. *Quaternary Geochronology*, 6(3-4), 407-422. <https://doi.org/10.1016/j.quageo.2011.03.010>

Munyikwa, K., Rittenour, T. M., and Feathers, J. K. 2017: Temporal constraints for the Late Wisconsinan deglaciation of western Canada using eolian dune luminescence chronologies from Alberta. *Palaeogeography, palaeoclimatology, palaeoecology*, 470, 147-165. <https://doi.org/10.1016/j.palaeo.2016.12.034>

Nishiizumi, K., Imamura, M., Caffee, M. W., Southon, J. R., Finkel, R. C., and McAninch, J. 2007: Absolute calibration of ¹⁰Be AMS standards. *Nuclear Instruments and Methods in Physics Research Section B: Beam Interactions with Materials and Atoms*, 258(2), 403-413. <https://doi.org/10.1016/j.nimb.2007.01.297>

Osmaston, H.A., 2006. Should Quaternary sea-level changes be used to correct glacier ELAs, vegetation belt altitudes and sea level temperatures for inferring climate changes? *Quaternary Research*, 65(2), 244-251. <https://doi.org/10.1016/j.yqres.2005.11.004>

Peltier, W.R., Argus, D.F. and Drummond, R. 2015: Space geodesy constrains ice-age terminal deglaciation: the global ICE-6G_C (VM5a) model. *Journal of Geophysical Research*, 120, 450-487. <https://doi.org/10.1002/2014JB011176>

Plug, L.J., Gosse, J.C., McIntosh, J.J. and Bigley, R. 2007: Attenuation of cosmic ray flux in temperate forest. *Journal of Geophysical Research: Earth Surface*, 112(F2). <https://doi.org/10.1029/2006JF000668>

Reimer, P.J., Austin, W.E.N., Bard, E. and Ramsey, C. 2020: The IntCal20 Northern Hemisphere radiocarbon age calibration curve (0-55 kcal BP). *Radiocarbon* 62(4). <https://doi.org/10.1017/RDC.2020.41>

Ritchie, J.C. 1976: The late-Quaternary vegetational history of the western interior of Canada. *Canadian Journal of Botany*, 54(15), 1793-1818. <https://doi.org/10.1139/b76-194>

Staiger, J., Gosse, J., Toracinta, R., Oglesby, B., Fastook, J. and Johnson, J.V. 2007: Atmospheric scaling of cosmogenic nuclide production: climate effect. *Journal of Geophysical Research: Solid Earth*, 112(B2). <https://doi.org/10.1029/2005JB003811>

Tarasov, L., Dyke, A.S., Neal, R.M. and Peltier, W.R. 2012: A data-calibrated distribution of deglacial chronologies for the North American ice complex from glaciological modelling. *Earth and Planetary Science Letters* 315, 30-40. <https://doi.org/10.1016/j.epsl.2011.09.010>

Williams, G.P. 1956 Study of snow density across Canada. NRCan Publication, 1956-08-01.

Wolfe, S., Huntley, D., and Ollerhead, J. 2004: Relict late Wisconsinan dune fields of the northern Great Plains, Canada. *Géographie physique et Quaternaire*, 58(2-3), 323-336. <https://doi.org/10.7202/013146ar>

Zimmerman, S.G., Evenson, E.B., Gosse, J.C. and Erskine, C.P. 1994: Extensive boulder erosion resulting from a range fire on the type-Pinedale moraines, Fremont Lake, Wyoming. *Quaternary Research*, 42(3), 255-265. <https://doi.org/10.1006/qres.1994.1076>

Figure S1. Photographs of boulders sampled for ^{10}Be surface exposure ages.





Figure S2. Probability density functions (i.e. ‘normal kernel density estimate’) for all ^{10}Be surface exposure samples sites. Blue lines represent reported age and 1 SD uncertainty, black lines are summed probabilities. Vertical black line represents the mean and grey boxes 1 SD excluding outliers of each sample site. Average ages, in bold, with propagated uncertainty calculated using the default calibration set of Borchers et al. (2016) and the time dependent ‘LSDn’ production scaling scheme of Lifton et al. (2014), with no correction for snow shielding and a zero erosion rate.

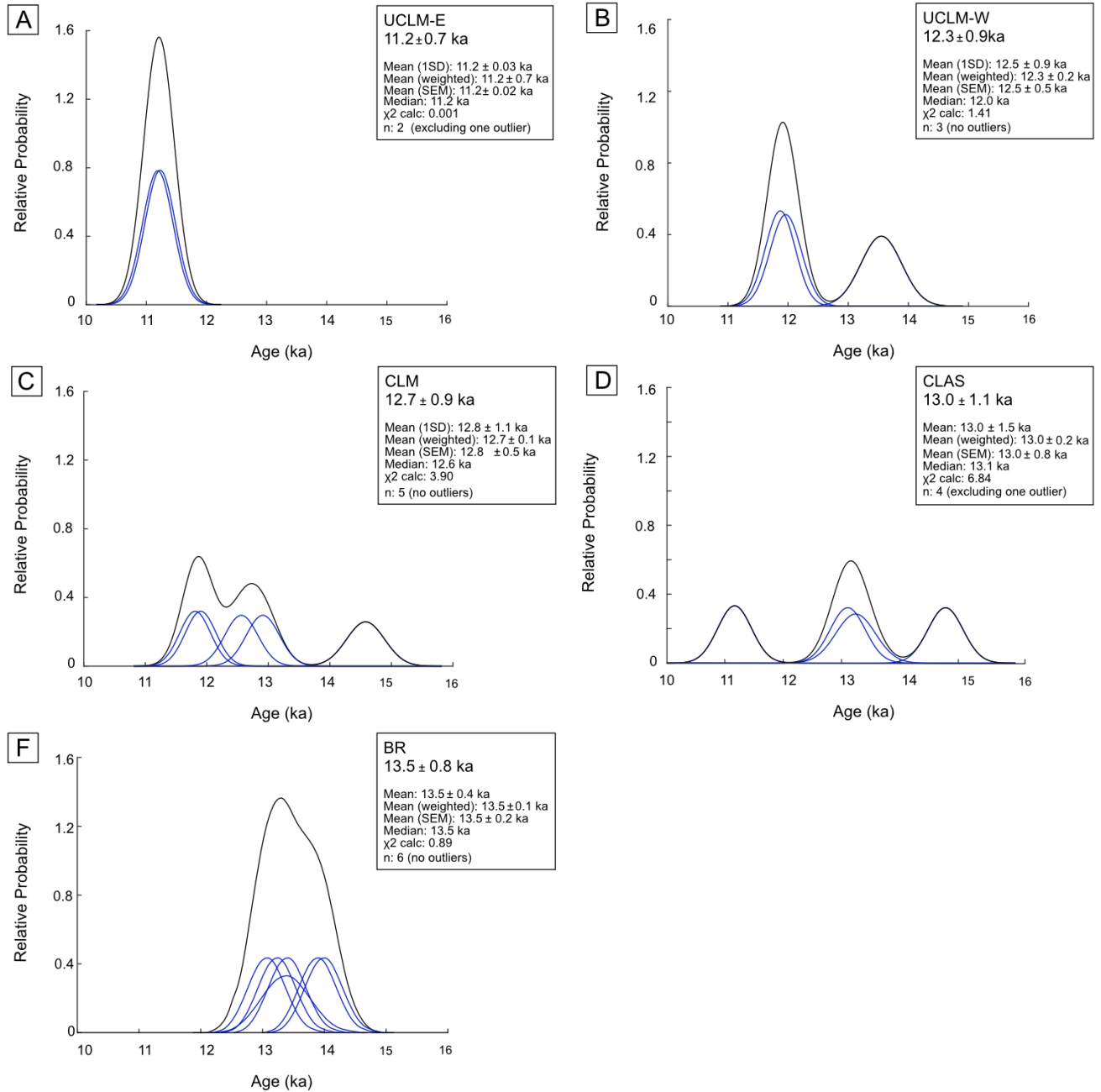


Figure S3. Bayesian age model output from OxCal v.4.4 (Bronk Ramsey, 2009a), using the IntCal20 calibration curve (Reimer et al., 2020) applied to the manually vetted radiocarbon, luminescence, and cosmogenic ages from the southwestern Laurentide Ice Sheet. The unmodelled (likelihood) probabilities are light grey, with modelled (posterior) probabilities in dark grey. Thick bar underlying the probability distributions is the 2-sigma confidence interval. Agreement indices (A:x) show probability of individual dates agreeing with the model.

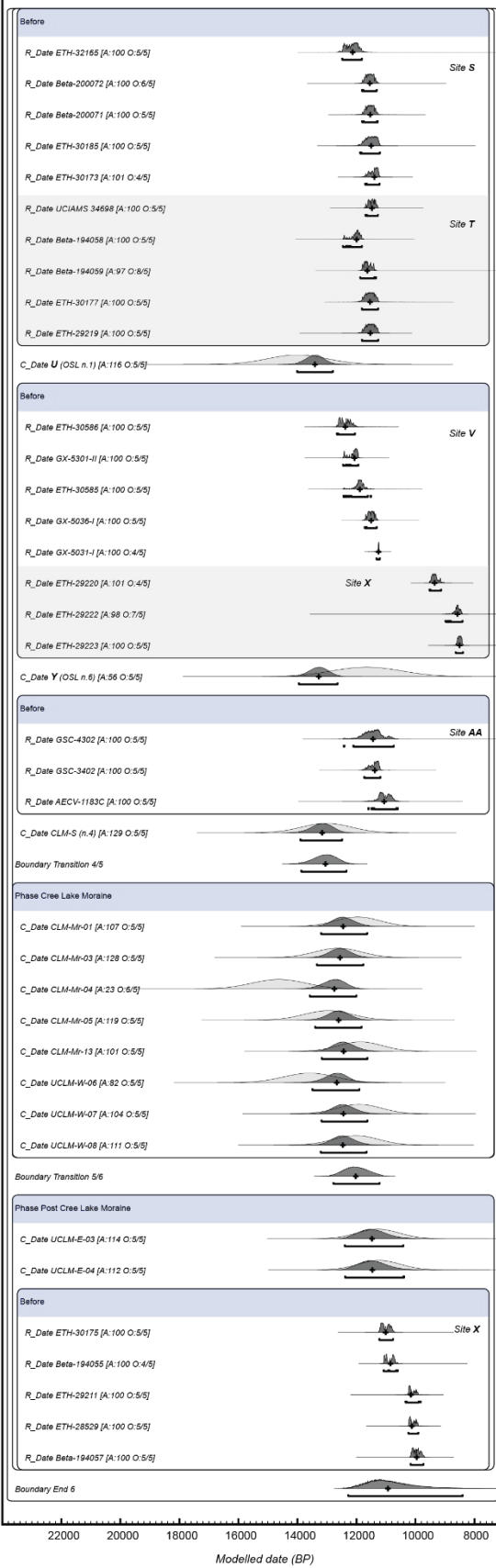
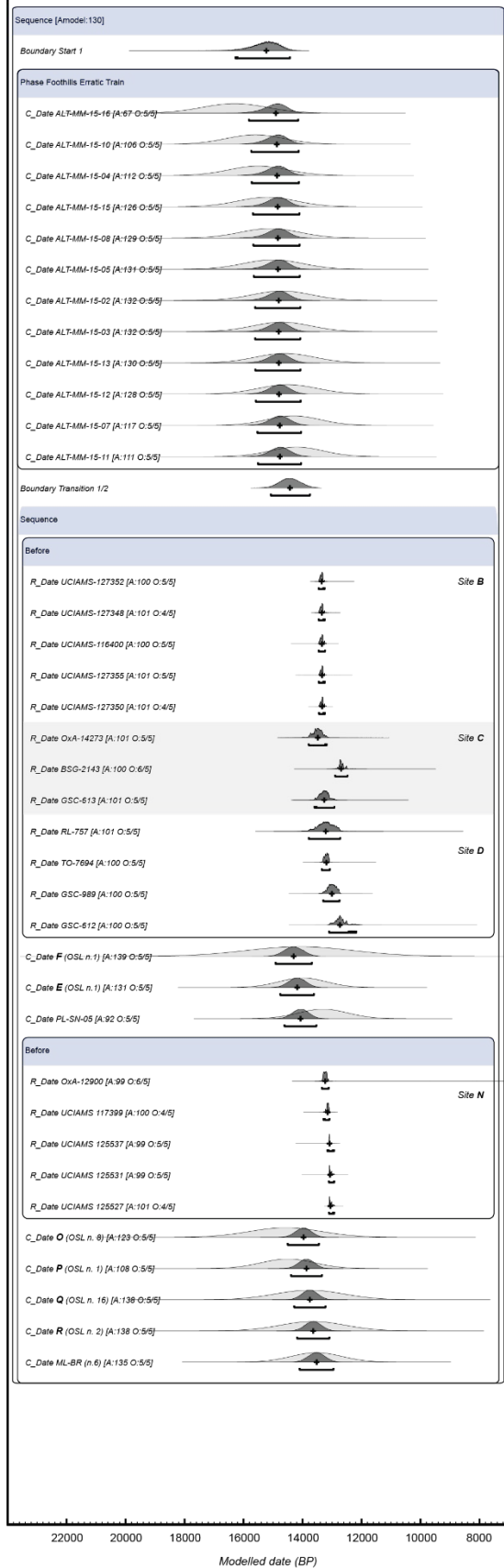


Table S1. Cosmogenic ^{10}Be sample details and modelled surface exposure ages

Laboratory no.	Sample ID	Latitude (DD)	Longitude (DD)	Modern elevation (m a.s.l.)	Palaeo-elevation (m a.s.l.) ^a	Palaeo-elevation (m a.s.l.) ^b	Boulder height (m)	Sample thickness (cm)	Quartz Mass (g)	Be carrier mass (g)	$^{10}\text{Be}/^9\text{Be}$ (10^{-14})	$^{10}\text{Be} \pm 1\sigma$ (atoms g^{-1} SiO_2)	^{10}Be age ^c (ka)	10Be age ^d (ka)	^{10}Be age ^e (ka)
JG3829	PL-SN-01*	52.1622	-113.5128	927	890	898	0.7	2	20.2010	0.2504	6.56	56602 ± 1607	5.8 ± 0.2	6.0 ± 0.2	6.0 ± 0.2
JG3830	PL-SN-02*	52.1622	-113.5127	927	890	898	0.8	2	20.0614	0.2103	7.51	54769 ± 1976	5.7 ± 0.2	5.8 ± 0.2	5.9 ± 0.2
JG3831	PL-SN-03*	52.1621	-113.5127	926	889	897	1.6	2	25.0204	0.8262	13.16	80616 ± 1695	8.3 ± 0.2	8.5 ± 0.2	8.4 ± 0.2
JG3832	PL-SN-05*	52.1607	-113.5440	976	939	951	0.8	2	25.1980	0.8199	21.60	130685 ± 2587	12.9 ± 0.3	13.3 ± 0.3	13.3 ± 0.3
JG3826	ML-BR-01	54.2769	-109.0520	496	464	470	0.7	3	20.0280	0.208	12.48	90900 ± 2205	13.5 ± 0.3	13.9 ± 0.3	13.9 ± 0.3
JG3827	ML-BR-02	54.2770	-109.0521	492	460	467	0.8	2.5	20.0498	0.2109	11.93	88020 ± 2402	13.1 ± 0.4	13.5 ± 0.4	13.5 ± 0.4
JG3612	ML-BR-03	54.2769	-109.0535	492	460	467	1	3	30.0720	0.2087	17.78	87398 ± 1848	13.1 ± 0.3	13.5 ± 0.3	13.4 ± 0.3
JG3613	ML-BR-04	54.2768	-109.0540	501	469	476	1.3	3	27.6640	0.1994	18.03	92033 ± 1943	13.6 ± 0.3	14.1 ± 0.3	14.0 ± 0.3
JG3614	ML-BR-06	54.3168	-109.5247	490	458	469	1	3	20.2070	0.212	12.04	85866 ± 1965	12.9 ± 0.3	13.2 ± 0.3	13.2 ± 0.3
JG3828	ML-BR-07	54.3179	-109.5248	526	494	502	1.6	3	20.0501	0.211	11.85	87450 ± 2179	12.7 ± 0.3	13.0 ± 0.3	13.0 ± 0.3
JG3602	CLM-S-02	56.8340	-109.0767	455	401	408	0.8	2.5	15.2180	0.206	11.62	106578 ± 2095	16.3 ± 0.3	17.1 ± 0.3	16.9 ± 0.3
JG3603	CLM-S-03	56.8344	-109.0761	457	403	413	0.7	3.5	20.2939	0.2065	9.71	69762 ± 1890	10.7 ± 0.3	11.2 ± 0.3	11.1 ± 0.3
JG3604	CLM-S-04	56.9179	-108.9774	432	376	382	1	3	20.2990	0.2064	11.24	80821 ± 2165	12.6 ± 0.3	13.3 ± 0.4	13.2 ± 0.4
JG3605	CLM-S-05*	56.9178	-108.9780	425	369	373	0.5	2	27.6148	0.2134	16.56	90659 ± 1910	14.2 ± 0.3	15.0 ± 0.3	14.8 ± 0.3
JG3606	CLM-S-06	56.9179	-108.9780	425	369	373	0.5	2.5	20.1880	0.2070	10.99	79711 ± 1897	12.5 ± 0.3	13.2 ± 0.3	13.0 ± 0.3
JG3607	CLM-Mr-01	57.5234	-109.3115	566	497	510	1.2	1.5	30.0719	0.2141	16.63	83839 ± 1766	11.4 ± 0.3	12.1 ± 0.3	12.0 ± 0.3
JG3608	CLM-Mr-03	57.5233	-109.3106	569	500	515	0.7	1.5	27.5660	0.2022	17.04	88465 ± 1866	12.0 ± 0.3	12.8 ± 0.3	12.6 ± 0.3
JG3609	CLM-Mr-04	57.3490	-109.2239	554	493	507	0.5	2	20.2944	0.2059	14.08	101095 ± 2170	14.0 ± 0.3	14.8 ± 0.3	14.6 ± 0.3
JG3610	CLM-Mr-05	57.3500	-109.2241	562	501	515	0.5	1.5	30.0501	0.2067	18.61	90668 ± 1868	12.4 ± 0.3	13.1 ± 0.3	13.0 ± 0.3
JG3611	CLM-Mr-13	57.5237	-109.3104	573	504	514	0.3	2	30.1446	0.2076	17.11	83457 ± 1758	11.3 ± 0.2	12.1 ± 0.3	11.9 ± 0.3
JG3615	UCLM-E-03	58.4685	-110.1993	285	207	217	1.6	4	27.5495	0.1992	11.59	59225 ± 1336	10.7 ± 0.2	11.6 ± 0.3	11.3 ± 0.3
JG3616	UCLM-E-04	58.4688	-110.2001	281	203	216	1	4	30.0464	0.2061	12.12	58797 ± 1336	10.7 ± 0.2	11.6 ± 0.3	11.2 ± 0.3
JG3617	UCLM-E-05*	58.4678	-110.1981	283	205	218	1.3	4	27.5301	0.2004	16.15	83232 ± 1761	15.1 ± 0.3	16.3 ± 0.3	16.0 ± 0.3

JG3618	UCLM-W-06	58.1798	-110.4310	315	250	263	0.6	4	30.0209	0.2088	14.99	73800 ± 1839	13.0 ± 0.3	13.9 ± 0.3	13.6 ± 0.3
JG3619	UCLM-W-07	58.1807	-110.4298	344	279	288	1	4	27.5892	0.2035	12.82	66875 ± 1412	11.4 ± 0.2	12.2 ± 0.3	11.9 ± 0.3
JG3620	UCLM-W-08	58.1807	-110.4296	335	270	279	1.3	4	27.5556	0.2132	12.22	66859 ± 1432	11.5 ± 0.2	12.3 ± 0.3	12.0 ± 0.3

Notes: Rock density for all samples is 2.6 g cm⁻³; no shielding correction applied to samples; exposure ages were calculated using the online calculator formerly known as CRONUS (Balco et al., 2008; v3.0; constants 3.0.3)

*Statistical outliers excluded from site mean ages

^a Palaeo-elevation derived using a GIA correction using numerical model simulations of Tarasov et al. (2012)

^b Palaeo-elevation derived using a GIA correction using numerical model simulations of Lambeck et al. (2017)

^c Ages (reported with 1σ internal error), calculated using the CRONUS default production rate (Borchers et al., 2016), Lm scaling (Lal, 1991/Stone, 2000) and modern-day elevations

^d Ages (reported with 1σ internal error), calculated using the CRONUS default production rate (Borchers et al., 2016), Lm scaling (Lal, 1991/Stone, 2000) and glacioisostatic palaeo-elevations.

^e Ages (reported with 1σ internal error), calculated using the CRONUS default production rate (Borchers et al., 2016), LSDn scaling (Lifton et al., 2014) and glacioisostatic palaeo-elevations.

Table S2. Summary statistics for ^{10}Be surface-exposure age distributions

Data Set	N	N_{removed}	Mean age (ka)	$\pm 1\sigma$ (ka)	Propagated uncertainty (ka)	Error-weighted mean (ka)	Standard error of the weighted mean (ka)	Weighted standard deviation (ka)	Median age (ka)	χ^2 calculated	χ^2 expected (95%)	χ^2 test (Pass/Fail)
UCLM-E (outliers)	3	-	12.8	2.7	1.6	12.3	0.2	1.6	11.3	11.64	5.99	Fail
UCLM-E (no outliers)	2	1	11.2	0.03	0.7	11.2	0.2	0.02	11.2	0.001	3.84	Pass
UCLM-W (no outliers)	3	-	12.5	0.9	0.9	12.3	0.2	0.5	12.0	1.41	5.99	Pass
CLM (no outliers)	5	-	12.8	1.1	0.9	12.7	0.1	0.5	12.6	3.90	9.49	Pass
CLAS (outliers)	5	-	13.8	2.2	1.3	13.7	0.1	1.0	13.2	13.90	9.49	Fail
CLAS (no outliers)	4	1	13.0	1.5	1.1	13.0	0.2	0.8	13.1	6.84	7.82	Pass
BR (no outliers)	6	-	13.5	0.4	0.8	13.5	0.1	0.2	13.5	0.89	11.07	Pass